Response of Coastal California Hydroclimate to the Paleocene-Eocene Thermal Maximum

Xiaodong Zhang[1*], Brett J. Tipple[2], Jiang Zhu[3], William D. Rush[4], Christian A. Shields[3], Joseph B. Novak[5], James C. Zachos[1]

[1]Department of Earth and Planetary Sciences, University of California, Santa Cruz, CA 95064, USA

[2]FloraTrace Inc., Salt Lake City, UT 84103, USA

[3]Climate and Global Dynamics Laboratory, National Center for Atmospheric Research, Boulder, CO 80307, USA

[4]Department of Environmental Studies and Sciences, Santa Clara University, Santa Clara, CA 95053, USA

[5]Department of Ocean Sciences, University of California, Santa Cruz, CA 95064, USA

**Correspondence to*: Xiaodong Zhang (xzhan335@ucsc.edu)

Abstract. The effects of anthropogenic warming on the hydroclimate of California are becoming more pronounced, with increased frequency of multi-year droughts and flooding. As a past analog for the future, the Paleocene-Eocene Thermal Maximum (PETM) is a unique natural experiment for assessing global and regional hydroclimate sensitivity to greenhouse gas warming. Globally, extensive evidence (i.e., observations, climate models with high pCO_2) demonstrates hydrological intensification with significant variability from region to region (i.e., dryer or wetter, or greater frequency and/or intensity of extreme events). Central California (paleolatitude ~42°N), roughly at the boundary between dry subtropical highs and mid-latitude low pressure systems, would have been particularly susceptible to shifts in atmospheric circulation and precipitation patterns/intensity. Here, we present new observations and climate model output on regional/local hydroclimate responses in central California during the PETM. Our findings based on multi-proxy evidence within the context of model outputs suggest a transition to an overall drier climate punctuated by increased precipitation during summer months along the central coastal California during the PETM.

1 Introduction

Global warming of a few degrees celsius over the next century is projected to intensify the hydrological cycle on a range of temporal and spatial scales, manifested primarily by amplified wet-dry cycles (Held and Soden, 2006; Douville et al., 2021). Indeed, just over last few decades there has been an increasing frequency in the severity of extremes characterized by compound heat waves and intense drought (Büntgen et al., 2021; Williams et al., 2020; Zscheischler and Lehner, 2022), and/or heavy precipitation and flooding (Liu et al., 2020; Risser and Wehner, 2017). As greenhouse gas driven warming continues, such precipitation extremes (wet or dry) are expected to intensify (Stevenson et al., 2022). This is particularly so for California which receives much of its rainfall from winter systems fueled by atmospheric rivers (AR), the frequency of which are forecast to decline as the systems shift northward (Simon Wang et al., 2017). The decline in winter precipitation along with warming will create more intense droughts even as the potential for extreme precipitation events increases (Vogel et al., 2020; Swain et al., 2018).

Climate model predictions for intensification of the hydrological cycle are supported by case studies of extreme warming events of the deep past (Carmichael et al., 2017). In particular, the Paleocene-Eocene Thermal Maximum (PETM) has emerged as a unique natural experiment for assessing global and regional hydroclimate sensitivity to greenhouse gas warming (Zachos et al., 2008). Extensive evidence exists for a major mode shift of local/regional precipitation patterns and intensity (Pagani et al., 2006; Slotnick et al., 2012; Schmitz and Pujalte, 2003; Sluijs and Brinkhuis, 2009; Smith et al., 2007; Handley et al., 2012; Kozdon et al., 2020) including enhanced erosion and extreme flooding in fluvial sections (e.g., Pyrenees; Bighorn basin), and increased weathering and sediment fluxes to coastal basins (e.g., Bass River, Wilson Lake, mid-Atlantic coast; Mead Stream, New Zealand etc.) along with other observations (John et al., 2008; Nicolo et al., 2010; Stassen et al., 2012; Self-Trail et al., 2017; Wing et al., 2005; Kraus and Riggins, 2007; Foreman, 2014).

These observations of regional hydroclimate serve as the basis for climate model experiments forced with proxy-based estimates of ΔpCO_2 for the PETM (i.e., 3x-6x pre-industrial)(Kiehl and Shields, 2013; Carmichael et al., 2016; Zhu et al., 2020). Using such estimates, model simulations show an overall increase in poleward meridional water vapor transport as manifested by a net increase in evaporation of subtropical regions, balanced by higher precipitation of tropical/high latitudes characterizing the 'wet-gets-wetter and dry-gets-drier' hydrological response. The latest simulations using high-resolution climate models display several key regional responses including increased frequency of extreme precipitation events, especially the coastal regions where atmospheric rivers (AR) are common (Rush et al., 2021). Indeed, observations of high-energy flooding events in SW Europe (i.e., the Pyrenees) during the PETM (Schmitz and Pujalte, 2003) can be explained by increased frequency of North Atlantic ARs contributing landfall in that region. Pacific AR activity as simulated for the PETM also becomes more intense but less frequent along the central California coast by shifting northward with the storm tracks (Shields et al., 2021), not unlike the projections for California in the future (Shields and Kiehl, 2016; Massoud et al., 2019). This pattern is consistent with warming scenarios in general which have weakened zonal wind belts (i.e., the westerlies) that are shifting poleward (Abell et al., 2021; Douville et al., 2021).

Testing the theoretical response of extreme global warming on Pacific ARs and impacts on seasonal precipitation along North America's western coast in general is challenging and still limited by the lack of observations. Here we constrain the regional hydroclimate response along the central California coast during the PETM using several independent proxies (i.e., clay mineralogy, grain size distribution, $\delta^{13}C_{org}$ stratigraphy, and leaf wax $\delta^2H_{n\text{-alkane}}$ isotope records), which are either directly or indirectly sensitive to shifts in precipitation patterns/intensity. These proxies are then compared against Earth System model simulations of the greenhouse gas forced changes in regional precipitation (i.e., pattern/intensity). The new records complement data from a previous study (John et al., 2008), and along with the latest climate modeling experiments provide a unique case study of the sensitivity of regional hydroclimate to major greenhouse warming.

2 Materials and methods

2.1 Site Location

The studied outcrop section, Lodo Gulch, is part of the late Paleocene-early Eocene Lodo Formation located in the Panoche Hill of central California (Fig. 1). During the late Paleocene, the section was situated at a paleolatitude ~42°N, roughly at the boundary between the dry subtropical highs and mid-latitude low-pressure systems. The Lodo Formation is comprised primarily of siltstone with a relatively low abundance of calcareous microfossils truncated by thin glauconitic sand layers (Brabb, 1983). Depositional facies are consistent with neritic-bathyal setting along the outer shelf (John et al., 2008).

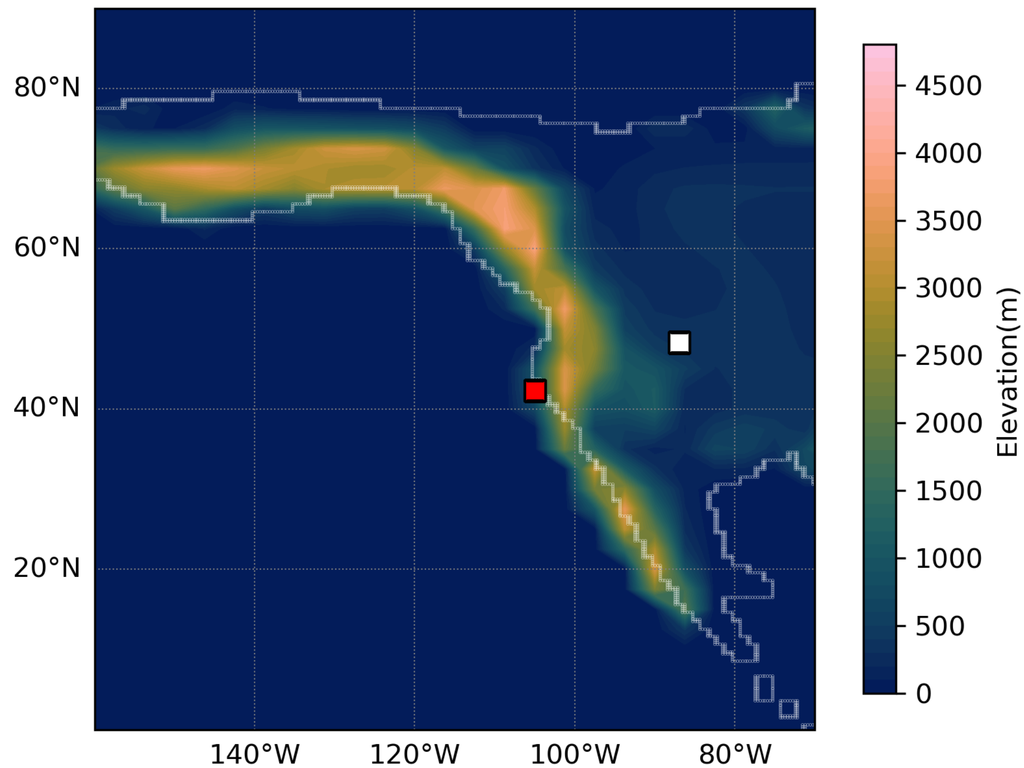

Figure 1. Paleogeography and location of the Lodo Gulch section (red square) along the Central California coast and Big Horn Basin (white square) in the North America continent for reference at 56 Ma. Late Paleocene-early Eocene topography boundary of North America was adapted from Lunt et al. (2017).

2.2 Methods

2.2.1 Bulk organic stable carbon isotopes

Sediment samples used for this study include those originally collected (ca. 28) by John et al. (2008). In addition, new samples (ca. 27) were collected from the upper Paleocene for organic C isotopic analyses ($\delta^{13}C_{org}$) to better establish pre-PETM baseline. Samples were analyzed in the UCSC Stable Isotope Laboratory using a CE instruments NC2500 elemental analyzer coupled with Thermo Scientific Delta Plus XP iRMS via a Thermo-Scientific Conflo III. All samples were calibrated with VPDB (Vienna PeeDee Belemnite) for $\delta^{13}C$ and AIR for $\delta^{15}N$ against an in-house gelatin standard reference material (PUGel). Analytical reproducibility precision is ± 0.1 ‰ for $\delta^{13}C$ and ± 0.2 ‰ for $\delta^{15}N$.

2.2.2 Grain Size analyses

Particle size was measured by laser diffraction using Beckman Coulter with Polarization Intensity Differential Scatter (PIDS) housed at UCSC (see supplemental information). For each sample, 2 to 5 mg of bulk sediment was powdered and through a 2-mm sieve following the protocols in Blott et al., (2004). A total of 39 samples were measured, each in duplicate or triplicate to ensure reproducibility.

2.2.3 Clay Assemblages analyses

Sample preparation followed a slightly modified version of Kemp et al., (2016). Roughly 5 to 10 g of sediment was powdered in a pestle and mortar and then placed in a Calgon (Sodium hexametaphosphate) solution on a shaker table for 72 hours. Samples were sorted through a 63 µm sieve while collecting the fluid with the <63 µm fraction. The collected fluid and suspended fine fraction (< 63 µm) were allowed to settle for a period determined by Stokes' Law to keep < 2µm size clay particles remaining in suspension. The fluid was then decanted and dried in the oven at 40°C. Approximately 150 mg clay of each sample were used to prepared oriented mounts for X-ray diffraction (XRD) analysis. A total of 38 clay samples were prepared from the Lodo Formation. The sample residues were measured on a Philips 3040/60 X'pert Pro X-ray diffraction instrument at UCSC. Clay species (i.e., Smectite, Ilite, Kaolinite, Chlorite) were identified based on peak positions and intensities representing each clay mineral.

2.2.4 Leaf wax distribution and carbon/hydrogen isotopic composition

Sediment extraction, compound isolation, and compound-specific isotope measurements were conducted following Tipple et al. (2011). Briefly, sediments were freeze-dried, powdered (~500 g), and extracted with dichloromethane (DCM): methanol (2:1, *v/v*) using a Soxhlet extractor.

Total lipid extracts were concentrated and then separated by column chromatography using silica gel. *N*-alkanes were further purified from cyclic and branched alkanes using urea adduction following Wakeham and Pease (2004). *N*-alkane abundances were determined using gas chromatograph (GC) with a flame ionization detector (FID). Isotope analyses were then performed using a GC coupled to an iRMS interfaced with a GC-C III combustion system or a High Temperature Conversion system for $\delta^{13}C$ and $\delta^{2}H$ analyses, respectively. 59 samples were processed with a fused silica, DB-5 phase column (30 m × 0.25 mm I.D., 0.25 μm film thickness) with helium as the carrier at a flow of 1.5ml/min. GC oven temperature program was 60-320°C @ 5°C/min and isothermal for 30 min. A Thermo Trace MS was used for detection with the mass spec scanning from 50-800 m/z or exclusively m/z of 191, 217, 218, 370, 372, 386, and 400 for single ion monitoring. Biomarkers were identified by elution time and mass spectra of in-house petroleum standards with published biomarker distributions (Peters et al., 2005).

$\delta^{13}C$ and $\delta^{2}H$ values are expressed relative to Vienna Pee Dee belemnite (VPDB) and Vienna Standard Mean Ocean Water (VSMOW). Individual *n*-alkane isotope ratios were corrected to *n*-alkane reference materials (for $\delta^{13}C$, C_{20}, C_{25}, C_{27}, C_{30}, and C_{38} of known isotopic ratio and for $\delta^{2}H$, "Mix A" from Arndt Schimmelmann, Indiana University) analyzed daily at several concentrations. In addition, H_2 reference gas of known isotopic composition was pulsed between sample *n*-alkane peaks to confirm if normalizations were appropriate. Standard deviations (SD) of *n*-alkane reference materials were $\pm 0.6‰$ for $\delta^{13}C$ and $\pm 6‰$ for $\delta^{2}H$.

2.2.5 Earth System Models

Climate simulations from two models were used in this paper for (1) comparison with leaf wax proxy data and (2) extreme events analyses. (1) Water isotope-enabled Community Earth System Model version 1.2 (iCESM1.2) simulates changes in climate and water isotopic composition during the PETM (Zhu et al., 2020) with a horizontal resolution of 1.9×2.5° in atmosphere and land, and a nominal 1 degree in the ocean and sea ice components. Water isotope capabilities have been incorporated into all the components of CESM 1.2 (Brady et al., 2019), which include the Community Atmosphere Model, version 5 (CAM5) for the atmosphere, the Parallel Ocean Program, version 2 (POP2) for the ocean, the Community Land Model, version 4 (CLM4) for the land, River Transport Model (RTM) for river flow, and Community Ice Code, version 4 for sea ice. All simulations were run with the identical boundary conditions (including early Eocene paleogeography, land-sea mask, vegetation distribution, and pre-industrial (PI) non-CO_2 greenhouse gas concentrations, soil properties, natural aerosol emissions, solar constant and orbital parameters) following the DeepMIP protocol (Lunt et al., 2017) and differ only in atmospheric CO_2 concentration. Crucially, the models with reduced latitudinal temperature gradients (e.g., GFDL, CESM) more closely reproduce proxy-derived precipitation estimates and other key climate metrics (Cramwinckel et al., 2023). Increased climate sensitivity with warming and cloud feedback in CESM1.2 over earlier models improved water vapor sensitivity. (2) Using the same CESM1.2 framework, high resolution (0.25°) simulations were conducted with forced sea surface temperatures (SSTs) and active atmosphere and land components (CAM5, CLM4). RTM was run at 1° resolution, and forced SST were calculated from consistent 2° fully coupled PETM simulations (see details in Rush et al., 2021 and reference therein). The much higher horizontal resolution in the atmosphere enables improved simulation of the extreme events. Hourly, daily (CAM5), and monthly (iCESM1.2) temporal resolution precipitation outputs from both sets of climate simulations were utilized in this paper, with 100 years taken from the equilibrated iCESM1.2 simulations, and 15 years from the forced SST high resolution CAM5 simulations.

3 Results

3.1 Bulk organic and *n*-alkane stable carbon isotopes

A carbon isotope excursion is present in both bulk organic (Fig. 2a) and carbonate based $\delta^{13}C$ records (John et al., 2008) across the P-E boundary, marking the PETM onset of the Lodo section. The terrestrial leaf wax *n*-alkane records all capture the carbon isotope excursion (CIE) with a pattern that roughly parallels the other published records (i.e., planktonic foraminifera) (John et al., 2008), though is much less noisy than the bulk $\delta^{13}C_{org}$ record, not unexpected given the potentially variable composition of the bulk organic matter. The magnitude of the $\Delta\delta^{13}C_{n\text{-alkane}}$ is roughly -4‰ (average of *n*-C_{27}, *n*-C_{29}, *n*-C_{31}) at the onset of the CIE, followed by a gradual recovery that is truncated at the disconformity between 20.3m and 23.5m (coincides with nannofossil biozone boundary NP10 and NP11), thus marking the top of the PETM body (Fig. 2a). The disconformity coincides with a global sea level regression (John et al., 2008). Following the recovery, above the disconformity, the mean $\delta^{13}C_{n\text{-alkane}}$ is depleted relative to the pre-PETM baseline as is observed in some other PETM sections (Cui et al., 2021; Garel et al., 2013; Hasegawa et al., 2006).

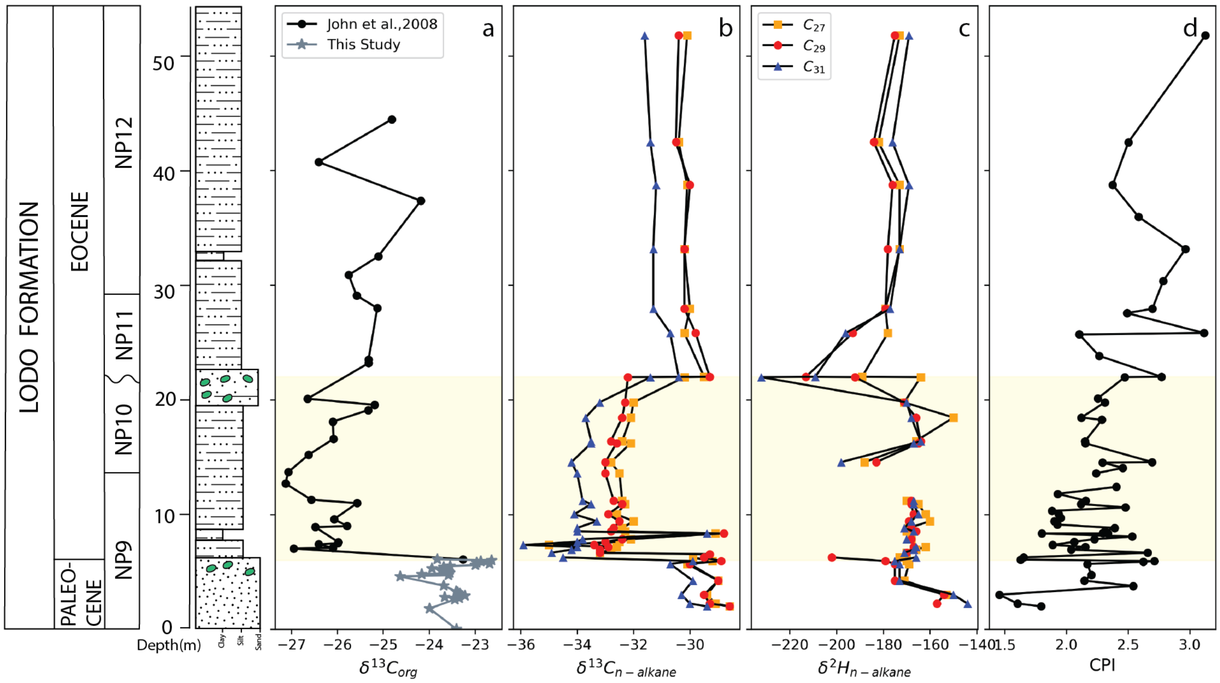

Figure 2. Terrestrial higher plant leaf wax *n*-alkane δ^{13}C and δ^{2}H records for the Lodo Gulch section, Central California. The shaded area represents the bounds of the CIE/PETM (a) bulk organic carbon isotope record. (b,c) leaf wax compound specific carbon/hydrogen isotope records in *n*-C_{27} (yellow square), *n*-C_{29} (red closed circle), *n*-C_{31} (blue triangle), (d) *n*-alkane carbon preference indices (CPI).

3.2 Hydrogen isotopes

The leaf wax $\delta^{2}H_{n\text{-alkane}}$ values range from -150 to -213‰ over the entire sampled section that has an initial decrease of 25‰ (from -150 to -175‰ in C_{29}) just prior to the CIE onset and then followed by a slight rise (~6 ‰) right after the onset. The relatively invariable $\delta^{2}H_{n\text{-alkane}}$ through the PETM is punctuated with two brief intervals of more negative values (-202‰ at 6.26m and -213‰ at 22m). The second larger anomaly coincides with the disconformity (related to local sea level regression). The post-PETM $\delta^{2}H_{n\text{-alkane}}$ values are on average lower than for the upper Paleocene/PETM, although analytical errors may bias the values. Given the limited number of samples to establish a baseline for the upper Paleocene, the significance of the pre (and post CIE) shifts/anomalies in $\delta^{2}H_{n\text{-alkane}}$ should be considered with some caution. Several other sections do show pre-CIE shifts, both positive and negative, and typically an enrichment with the CIE (Handley et al., 2008, 2011; Jaramillo et al., 2010; Tipple et al., 2011). Such minor changes likely reflect unconstrained orbital influences on regional precipitation (Rush et al., 2021; Campbell et al., 2024), especially considering the variable direction of change from location to location.

3.3 Clay assemblage and grain size

Clay assemblages and particle grain size should to some extent be influenced by regional hydroclimate. At Lodo, the clay assemblages (Fig. 3) are dominated by smectite throughout. The minor clay components illite and chlorite show several spikes relative to smectite within the lower (8 to 10 m) and upper CIE (~19 m), whereas the ratio of kaolinite gradually increases (0.5 to 1.5) only over the upper portion of the CIE (10 to 20 m). A delayed rise in kaolinite has also been observed in a few other PETM sections whereas some show an immediate rise (Tateo, 2020; Gibson et al., 2000). The smectite concentration and kaolinite/smectite ratio remain high in the post-PETM interval. The late Paleocene, with relative coarse sandy size, shows slight spikes of kaolinite associated with other minerals. Grain size, largely silt and clay, shows a distinct shift toward finer fractions (i.e., clay) with the onset of the CIE (Fig. 3e).

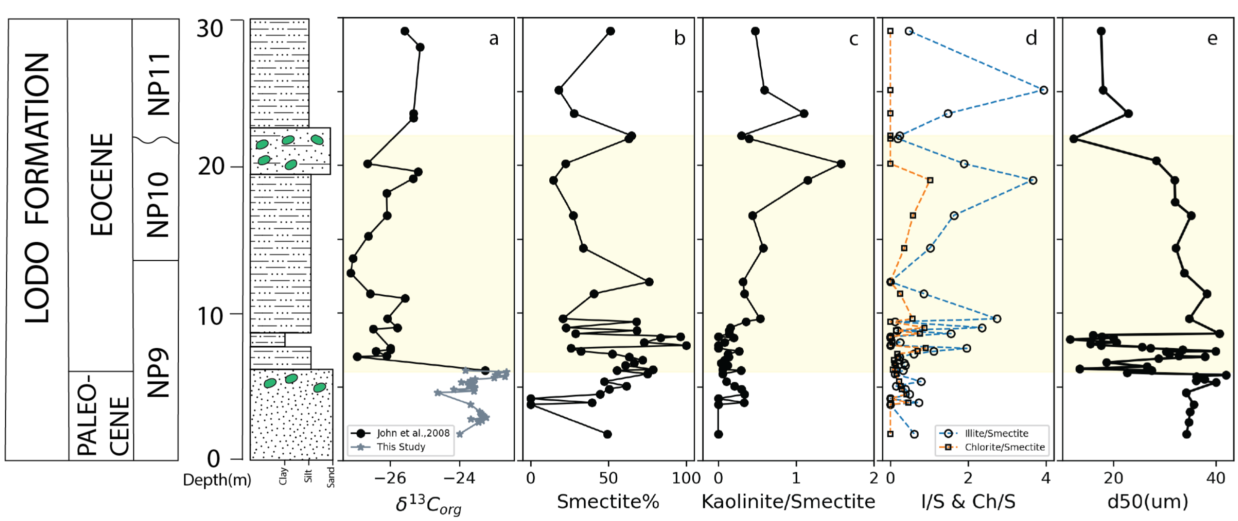

Figure 3. Integrated C isotope and clay assemblage records for the Lodo Gulch section, central California (a) bulk organic carbon isotope, (b,c,d,e) clay assemblage ratios, (e) decreasing mean particle size (D50: 50% of the total particle size in sediments) corresponds to CIE onset.

3.4 Earth system model simulations

We obtained and processed temperature and precipitation output from two community earth system/climate models: the isotope-enabled iCESM1.2 and high-resolution CAM5 models (daily precipitation over 15 years) forced by a range of greenhouse conditions (1x,3x,6x,9x $p\mathrm{CO_2}$ pre-industrial), both with Eocene paleogeography. For comparisons with observations, we used output from the 3x to 6x $p\mathrm{CO_2}$ simulations which best replicated the observed SST (ΔSST) for the pre-PETM and PETM (Zhu et al., 2020). Overall, monthly winter precipitation for the study region decreases (~30%) during the PETM in both simulations with a slight increase in the summer (Fig. 4,5). CAM5 output shows a modest decrease in mean annual precipitation with significant seasonal shifts during the PETM (Fig. 5a). Seasonal changes of monthly averaged δ^{18}O and δ^{2}H from mean monthly precipitation in iCESM1.2 of central California are consistent with CAM5. On average the $\delta^{2}H_{precip}$ increases by ca. 5-10 ‰ from pre-PETM to PETM, especially in the winter/spring, with a smaller shift in summer/fall (1~2 ‰) (Fig 4. a,b,c). The Extreme value index (ξ), a representation of the distribution of exceedance right tail (supplemental information), shows a small but statistically robust increase in wet extremes of winter (DJF) with a significant increase in summer (JJA) during the PETM (Fig. 5b).

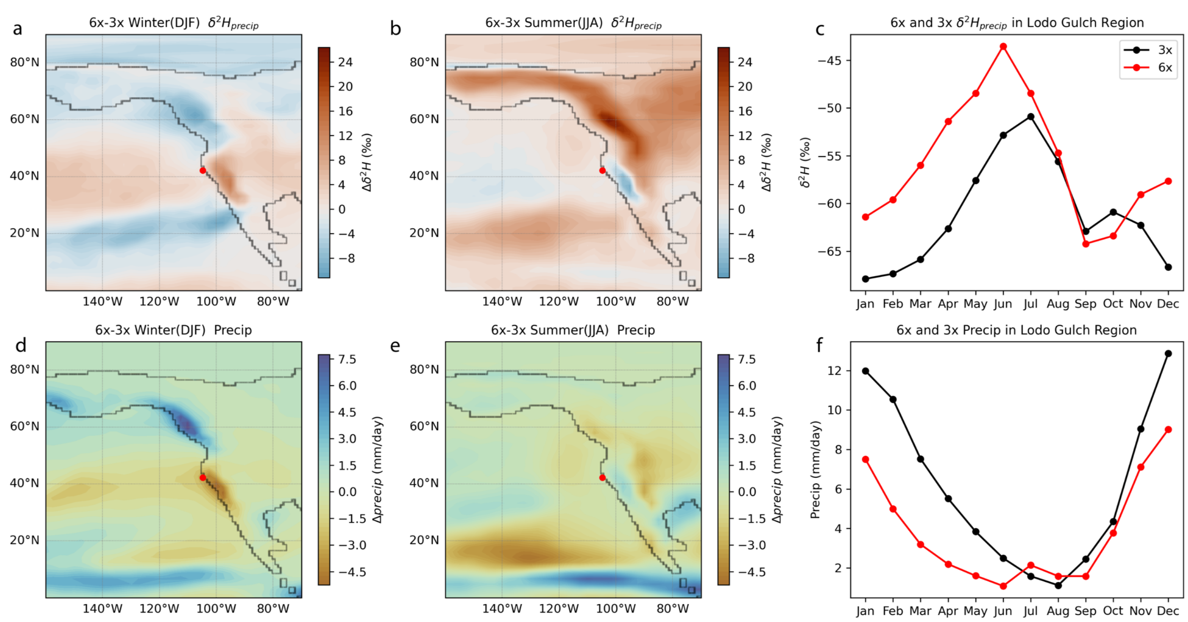

Figure 4. Seasonal and monthly meteoric precipitation amounts (mm/day) and H-isotopic composition for the North Pacific/Western N. America as simulated with the iCESM1.2 (Zhu et

al., 2020) under pre-PETM (3x in black) and PETM (6x in red) pCO_2 forcing. Panels (a) and (b) show $\Delta\delta^2H_{precip}$ between pre-PETM (3x) and PETM (6x) in winter (DJF) and summer (JJA). Panel (c) shows the annual seasonal cycle of δ^2H_{precip} for central California (pre-PETM in black, PETM in red). Mean daily precipitation rate difference for (d) winter and (e) summer between pre-PETM (3x) and PETM (6x). Panel (f) shows the annual seasonal cycle of daily precipitation rate for central California. Values represent the area-weighted average over 4° x 4° box bounding the study site.

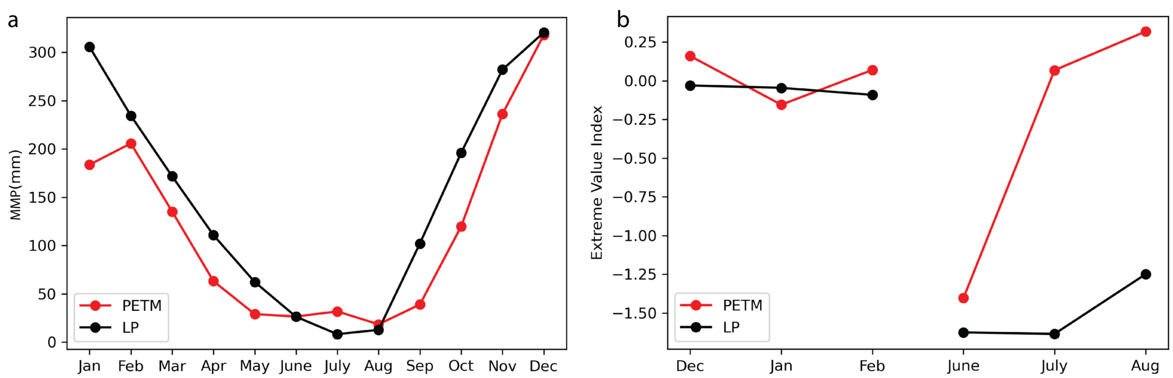

Figure 5. High resolution CAM5 model output (Shields et al., 2021) of (a) mean monthly precipitation for central California over 15 model years for the Late Paleocene/LP under low pCO_2 (680 ppmv) and for the PETM under high pCO_2 (1590ppmv). (b) Extreme value index (ξ) comparison of mean monthly precipitation in winter and summer of central California region based on the CAM5 precipitation outputs.

4 Discussion

4.1 Hydroclimate response from model simulations.

In all model simulations of the PETM forced with higher pCO_2 (e.g., 3x to 6x pre-industrial), the hydrological cycle intensifies as manifested by increases in global mean precipitation and meridional vapor transport (Kiehl and Shields, 2013; Kiehl et al., 2018; Carmichael et al., 2016; Zhu et al., 2020). Regionally however, the magnitude and even the sign of precipitation change can differ considerably from global means (Carmichael et al., 2016, 2017). This is most evident in the latest low and high-resolution model simulations of the PETM (Zhu et al, 2020; Shields et al., 2021). For central California, the simulations yield an overall decline in mean annual precipitation mainly due to a notable decline in winter precipitation with only a slight increase in summer (Fig. 4). This pattern is produced by both the water isotope-enabled iCESM1.2 and the higher resolution CAM5 with an overall shift into lower amplitude seasonal cycles (i.e., drier winter/spring and a slightly wetter summer) (Fig. 4, 5). This seasonal wet-dry shift appears to be driven in part by a pronounced northward shift of atmospheric rivers (ARs) in winter along the North American Pacific coastline (Shields et al., 2021). As ARs deliver most of the winter precipitation to the mid-latitude Pacific coast, less frequent occurrences result in drier winters during the PETM. Moreover, the extreme value index (ξ) shows a small but statistically robust increase in winter (DF) wet extremes with a significant increase in the probability of summer (JJA) wet exceedance during PETM (Fig. 5b). The latter might be due to elevated tropical storm activity along the Pacific coast during PETM (Fig. S7; Kiehl et al., 2021).

4.2 Hydroclimate response from observations.

4.2.1 Sedimentation rate, clay assemblages and grain size distribution

Arguably, the collection of observations from Lodo (i.e, sediment flux, clay assemblages, and leaf wax δ^2H isotopes), within limitations, appear to be mostly consistent with the model output. Starting with siliciclastic sedimentation, rates should be highly susceptible to a major shift in hydrologic conditions as changes in the seasonality of precipitation (along with vegetative cover) would impact rates of erosion and sediment transport. The coarse resolution of stratigraphic control at Lodo does limit the ability to constrain changes in sedimentation rates in detail. However, just considering the thickness of the CIE (~10 m), one could argue for a shift toward higher seasonality of precipitation with overall drier conditions as suggested by John et al., (2008).

The other constraints on regional precipitation would also support a shift toward drier conditions. For example, an increase in the relative abundance of kaolinite fluxes has been widely observed across the CIE onset in many PETM sections from mid to high latitudes (Tateo, 2020; Gibson et al., 2000) and interpreted as evidence of a major mode shift in local hydroclimates. In contrast, the clay mineralogy (Fig. 3) for the Lodo Formation is dominated mainly by smectite at the onset of the PETM, consistent with seasonal wet/dry cycles under warm conditions (Gibson et al., 2000). A subtle increase in the kaolinite/smectite could be interpreted as evidence of higher humidity (Gibson et al., 2000). However, the skewed grain size distribution of clay sediments around 8 m coinciding with illite/smectite peaks (Fig. 3e and S1) indicate higher fluvial velocity and increased erosion as observed elsewhere (Chen et al., 2018; Foreman et al., 2012; Foreman, 2014). For example, along the mid-Atlantic margin it appears the kaolinite might have been exhumed from local Cretaceous laterites (Lyons et al., 2019). The regionally enhanced physical weathering and erosion could be related to an increase in the frequency of episodic wet/dry extremes during the PETM as simulated by models.

4.2.2 Precipitation and Leaf wax $\delta^2H_{n\text{-alkane}}$

The Lodo leaf wax $\delta^2H_{n\text{-alkane}}$ record at first glance is somewhat equivocal in terms of the response of local hydroclimate. In theory, terrestrial higher plant $\delta^2H_{n\text{-alkane}}$ should provide insight into changes in regional precipitation amounts/source, particularly major mode shifts (Jaramillo et al., 2010; Pagani et al., 2006; Tipple et al., 2011). In some PETM records, $\delta^2H_{n\text{-alkane}}$ significantly increases, consistent with the effects of higher T on water isotope fractionation. For example, in the Arctic, $\delta^2H_{n\text{-alkane}}$ records show a positive excursion of 55‰ at CIE onset, consistent with higher T, a reduced meridional temperature gradient and decreasing isotope distillation during vapor transport (Pagani et al., 2006). However, there are notable exceptions. In some subtropical/mid-latitude sites, $\delta^2H_{n\text{-alkane}}$ decreases (ca ~20‰) across the onset of PETM (Handley et al., 2008, 2011; Jaramillo et al., 2010; Tipple et al., 2011). In comparison, Lodo $\delta^2H_{n\text{-alkane}}$ displays a comparatively muted response, showing a slight ^2H enrichment in the main body PETM followed by several anomalous shifts toward more negative values (Fig. 2c).

Given the robust evidence for mode shifts in hydroclimate elsewhere during the PETM, does the relatively stable Lodo $\delta^2H_{n\text{-alkane}}$ record necessarily support a local/regional stable hydroclimate (i.e., in conflict with the modeling and other observations)? As H-isotope fractionation in plants is related to photosynthetic pathways, source water availability, and atmospheric humidity (Sachse et al., 2012; Tipple et al., 2015), it is possible that local shifts in meteoric water isotope composition were offset by another influencing factor(s). Regarding photosynthetic pathways, along the west coast of North America, no detailed records of vegetation response have been generated for the PETM. Still, for the late Paleocene and early Eocene intervals, Korasidis et al. (2022) found little deviation in the Koppen-Geiger climate type (i.e., Mediterranean) within the central California region. This evidence along with the lack of change in *n*-alkane average chain length (ACL) in the Lodo section (Fig S5) would suggest no major changes in vegetation assemblages during the PETM. Another factor, reworking of Paleocene terrestrial organic matter (e.g., Tipple et al., 2011), could possibly dampen of isotopic *n*-alkane signals at Lodo, although the CPI and the leaf wax carbon isotopes would suggest minimal reworking of the *n*-alkanes, as opposed to other coastal PETM sites where the evidence for reworking is robust (e.g., Lyons et al., 2019; Hollingsworth et al., 2024). As such, if we assume the $\delta^2H_{n\text{-alkane}}$ record reflects only on changes in local meteoric waters, the observed modest change of $\delta^2H_{n\text{-alkane}}$ values at Lodo could be interpreted in several ways in terms of T-related changes on isotope fractionation that were offset by changes in dominant season of precipitation, and/or vapor sources and distance of transport. For example, a shift in precipitation between winter and late summer/fall could offset the effects of warming assuming a shift from a proximal (north or central Pacific) to a more distal (Gulf of Mexico) source of vapor (Hu and Dominguez, 2015). At ground level, stronger evapo-transpiration during biosynthesis can isotopically be offset by external water source availability (i.e. seasonal precipitation). Local/regional ground water table variations caused by hydrological change would also affect the source water-use efficiency of plants since surface water tends to be more depleted in some perennial species after intense storms in the groundwater (Hou et al., 2008; Krishnan et al., 2014). Hydrogen isotope fractionation in plants can also be biased by seasonal shift in regional vegetation growth regime. For example, leaf wax lipids from terrestrial plants usually record hydrological conditions earlier in the season rather than fully integrating the entire growing season (Hou et al., 2008; Tipple et al., 2013). Finally, episodic extremes in precipitation may dominate the hydrogen isotopic composition of the leaf wax (Krishnan et al., 2014). If soil water is derived mainly from extreme events during the growth season, the lack of a major shift in the Lodo $\delta^2H_{n\text{-alkane}}$ record with the onset of the PETM could reflect a combination of more ^2H-depleted precipitation delivered by seasonal storms offset by warming induced ^2H-enrichment in leaf water.

4.3 Comparison of leaf water and modeled δ^2H

Assuming leaf wax δ^2H is primarily influenced by local meteoric water, how does the seasonal distribution of precipitation influence the bulk signal? In iCESM1.2 simulations with increasing pCO_2 (i.e., 3x to 6x pre-industry) and SST, the seasonal shifts in δ^2H of mean monthly precipitation from pre-PETM to PETM is significant. During the winter, as precipitation amounts decline, δ^2H_{precip} increases by 10‰ while decreasing by ~1 to 5‰ during late summer/fall in central California (Fig. 4). To estimate how this seasonal change of δ^2H_{precip} and precipitation amount influences leaf water δ^2H, we applied a leaf wax proxy model (supplemental information) which computes the combined effects of changes in seasonal precipitation and growing season length. The model shows leaf water δ^2H enriched ca. 4 to 7‰ from pre-PETM to PETM. Arguably, this would be consistent with minor ~6‰ enrichment observed in the Lodo record at the onset of the PETM. We also examined other sites for comparison of the predicted leaf water differences from pre-PETM to PETM with the fossil leaf wax $\Delta\delta^2H$ (see supplemental information) and find a similar pattern in other mid-latitude sites. Other factors to consider include precipitation source waters and a shift of a mixing endmember between proximal and distal sources of water in the coast. For example, with a summer shift of source water from the Pacific to subtropics (i.e., summer monsoons), the effect of increasing distance and distillation would isotopically deplete vapor (Hu and Dominguez, 2015), thus offsetting the temperature related enrichment of local δ^2H_{precip}. In addition, infrequent but high intensity tropical cyclones during the PETM (Kiehl et al., 2021) would tend to deliver relatively depleted precipitation (i.e., a more negative δ^2H) during summer months.

Finally, a related record that might indirectly reflect on precipitation amount (i.e., atmospheric humidity) is the magnitude of the CIE recorded by leaf wax $\delta^{13}C_{n\text{-alkane}}$. Recalcitrant higher plants leaf wax *n*-alkane carbon isotope ratios (n>25 with odd-over-even preference) reflect mainly carbon source (Diefendorf et al., 2010). However, photosynthetic carbon isotope fractionation (Δ_p) is sensitive to atmospheric pCO_2 variations, generally increasing with rising concentrations assuming a constant photosynthetic fractionation factor and humidity (Diefendorf et al., 2010). The $\delta^{13}C_{n\text{-alkane}}$ of Lodo section displays a sharp negative shift of ca. 4 ‰ (average of n-C_{27}, n-C_{29}, n-C_{31}) across the onset of CIE (Fig. 2b), which is consistent with global mean atmospheric CIE (Sluijs and Dickens, 2012) but generally smaller than observed in other leaf wax records (Handley et al., 2008, 2012; Jaramillo et al., 2010; Pagani et al., 2006; Tipple et al., 2011). The smaller $\delta^{13}C_{n\text{-alkane}}$ CIE recorded in Lodo would be consistent with a reduction in local humidity which should reduce the magnitude of Δ_p during photosynthetic carbon fixation.

Summary and Conclusions

Many sections globally exhibit evidence, often striking, of significant shifts in local hydroclimate at the onset of the PETM consistent with model simulations (e.g., 2x CO_2). These same models also simulate an overall decrease in winter precipitation for the central California coast due in large part to a reduction in AR frequency (Shields et al., 2021). While not as striking, the collection of observations from the central California Lodo Gulch Section would support a modest reduction in precipitation (i.e. MAP) during the PETM along with the possibility of an increase in the frequency of extreme precipitation events. This transition toward greater aridity and precipitation extremes is not unlike the forecasts for much of California over the coming centuries due to anthropogenic warming.

Data availability. Data tables of clay assemblages, grain size, organic carbon isotopes and leaf wax *n*-alkane stable isotopes will be available via the PANGAEA repository.

Author contribution. JCZ conceived the project design, acquired funding and provided overall supervision. XZ conducted stable isotope measurements, clay mineralogy, grain size analyses and iCESM/CAM5model output analyses. Leaf wax *n*-alkane carbon and hydrogen isotope measurements were performed by BJT. JBN conducted leaf wax proxy model experiments. CAS and WDR contributed to processing CAM model output. This paper was prepared by XZ with all authors contribution to the review and editing of the manuscript.

Competing interests. The authors declare that they have no conflict of interest.

Acknowledgements.
We thank Colin Carney (UCSC SIL) for technical support and acknowledge the contributions of Dr. Mark Pagani (deceased). Funding for this project has been provided by National Science Foundation No. OCE 2103513 to JCZ. All compound specific isotope analyses were performed at the Yale Institute for Biospheric Studies-Earth Systems Center that was supported by National Science Foundation Grant EAR 0628358 and OCE 0902993. The CESM project is supported primarily by the National Science Foundation (NSF). This material is based upon work supported by the National Center for Atmospheric Research, which is a major facility sponsored by the NSF under Cooperative Agreement No. 1852977.

References:

Abell, J. T., Winckler, G., Anderson, R. F., and Herbert, T. D.: Poleward and weakened westerlies during Pliocene warmth, Nature, 589, 70–75, https://doi.org/10.1038/s41586-020-03062-1, 2021.

Blott, S. J., Croft, D. J., Pye, K., Saye, S. E., & Wilson, H. E. Particle size analysis by laser diffraction. Geological Society, London, Special Publications, 232(1), 63-73, 2004.

Brabb, E. E.: Studies in Tertiary stratigraphy of the California Coast Ranges., US Geological Survey Professional Paper, 1213, 1983.

Brady, E., Stevenson, S., Bailey, D., Liu, Z., Noone, D., Nusbaumer, J., Otto-Bliesner, B. L., Tabor, C., Tomas, R., Wong, T., Zhang, J., and Zhu, J.: The Connected Isotopic Water Cycle in the Community Earth System Model Version 1, J Adv Model Earth Syst, 11, 2547–2566, https://doi.org/10.1029/2019MS001663, 2019.

Büntgen, U., Urban, O., Krusic, P. J., Rybníček, M., Kolář, T., Kyncl, T., Ač, A., Koňasová, E., Čáslavský, J., Esper, J., Wagner, S., Saurer, M., Tegel, W., Dobrovolný, P., Cherubini, P., Reinig, F., and Trnka, M.: Recent European drought extremes beyond Common Era background variability, Nat Geosci, 14, 190–196, https://doi.org/10.1038/s41561-021-00698-0, 2021.

Campbell, J., Poulsen, C. J., Zhu, J., Tierney, J. E., and Keeler, J.: CO_2-driven and orbitally driven oxygen isotope variability in the Early Eocene, Clim. Past, 20, 495–522, https://doi.org/10.5194/cp-20-495-2024, 2024.

Carmichael, M. J., Lunt, D. J., Huber, M., Heinemann, M., Kiehl, J., LeGrande, A., Loptson, C. A., Roberts, C. D., Sagoo, N., Shields, C., Valdes, P. J., Winguth, A., Winguth, C., and Pancost, R. D.: A model-model and data-model comparison for the early Eocene hydrological cycle, Climate of the Past, 12, 455–481, https://doi.org/10.5194/CP-12-455-2016, 2016.

Carmichael, M. J., Inglis, G. N., Badger, M. P. S., Naafs, B. D. A., Behrooz, L., Remmelzwaal, S., Monteiro, F. M., Rohrssen, M., Farnsworth, A., Buss, H. L., Dickson, A. J., Valdes, P. J., Lunt, D. J., and Pancost, R. D.: Hydrological and associated biogeochemical consequences of rapid global warming during the Paleocene-Eocene Thermal Maximum, https://doi.org/10.1016/j.gloplacha.2017.07.014, 2017.

Cramwinckel, M. J., Burls, N. J., Fahad, A. A., Knapp, S., West, C. K., Reichgelt, T., ... & Inglis, G. N. Global and zonal-mean hydrological response to early Eocene warmth. Paleoceanography and Paleoclimatology, *38*(6), e2022PA004542, 2023.

Chen, C., Guerit, L., Foreman, B. Z., Hassenruck-Gudipati, H. J., Adatte, T., Honegger, L., Perret, M., Sluijs, A., and Castelltort, S.: Estimating regional flood discharge during Palaeocene-Eocene global warming, Sci Rep, 8, 1–8, https://doi.org/10.1038/s41598-018-31076-3, 2018.

Cui, Y., Diefendorf, A. F., Kump, L. R., Jiang, S., & Freeman, K. H. Synchronous marine and terrestrial carbon cycle perturbation in the high arctic during the PETM. *Paleoceanography and Paleoclimatology*, *36*(4), e2020PA003942, 2021.

Diefendorf, A. F., Mueller, K. E., Wing, S. L., Koch, P. L., and Freeman, K. H.: Global patterns in leaf 13C discrimination and implications for studies of past and future climate, Proc Natl Acad Sci U S A, 107, 5738–5743, https://doi.org/10.1073/pnas.0910513107, 2010.

Douville, H., Raghavan, K., Renwick, J., and Allan, R.: Water Cycle Changes, Intergovernmental Panel on Climate Change 2021 – The Physical Science Basis, 1055–1210, https://doi.org/10.1017/9781009157896.010, 2021.

Foreman, B. Z.: Climate-driven generation of a fluvial sheet sand body at the Paleocene–Eocene boundary in north-west Wyoming (USA), Basin Research, 26, 225–241, https://doi.org/10.1111/BRE.12027, 2014.

Foreman, B. Z., Heller, P. L., and Clementz, M. T.: Fluvial response to abrupt global warming at the Palaeocene/Eocene boundary, Nature 2012 491:7422, 491, 92–95, https://doi.org/10.1038/nature11513, 2012.

Garel, S., Schnyder, J., Jacob, J., Dupuis, C., Boussafir, M., Le Milbeau, C.,. Paleohydrological and paleoenvironmental changes recorded in terrestrial sediments of the Paleocene-Eocene boundary (Normandy, France). Palaeogeography, Palaeoclimatology, Palaeoecology, 376, 184–199. https://doi.org/10.1016/j.palaeo.2013.02.035, 2013.

Gibson, T. G., Bybell, L. M., and Mason, D. B.: Stratigraphic and climatic implications of clay mineral changes around the Paleocene/Eocene boundary of the northeastern US margin, Sediment Geol, 134, 65–92, https://doi.org/10.1016/S0037-0738(00)00014-2, 2000.

Handley, L., Pearson, P. N., McMillan, I. K., and Pancost, R. D.: Large terrestrial and marine carbon and hydrogen isotope excursions in a new Paleocene/Eocene boundary section from Tanzania, Earth Planet Sci Lett, 275, 17–25, https://doi.org/10.1016/j.epsl.2008.07.030, 2008.

Handley, L., Crouch, E. M., and Pancost, R. D.: A New Zealand record of sea level rise and environmental change during the Paleocene-Eocene Thermal Maximum, Palaeogeogr Palaeoclimatol Palaeoecol, 305, 185–200, https://doi.org/10.1016/j.palaeo.2011.03.001, 2011.

Handley, L., O'Halloran, A., Pearson, P. N., Hawkins, E., Nicholas, C. J., Schouten, S., McMillan, I. K., and Pancost, R. D.: Changes in the hydrological cycle in tropical East Africa during the Paleocene-Eocene Thermal Maximum, Palaeogeogr Palaeoclimatol Palaeoecol, 329–330, 10–21, https://doi.org/10.1016/j.palaeo.2012.02.002, 2012.

Hasegawa, T., Yamamoto, S., & Pratt, L. M. Data report: Stable carbon isotope fluctuation of long-chain n-alkanes from Leg 208 Hole 1263A across the Paleocene/Eocene boundary. In D. Kroon, J. C. Zachos, & C. Richter, (Eds.), Proceedings of the Ocean Drilling Program: Scientific Results 208 (pp. 1–11). Ocean Drilling Program, 2006.

Held, I. M. and Soden, B. J.: Robust Responses of the Hydrological Cycle to Global Warming, J Clim, 19, 5686–5699, https://doi.org/10.1175/JCLI3990.1, 2006.

Hollingsworth, Emily H., Felix J. Elling, Marcus Peter Sebastian Badger, R. D. Pancost, A. J. Dickson, Rhian L. Rees-Owen, Nina Maria Papadomanolaki et al. Spatial and Temporal Patterns in Petrogenic Organic Carbon Mobilization During the Paleocene-Eocene Thermal Maximum, Paleoceanography and Paleoclimatology, 39, no. 2, 2024.

Hou, J., D'Andrea, W. J., and Huang, Y.: Can sedimentary leaf waxes record D/H ratios of continental precipitation? Field, model, and experimental assessments, Geochim Cosmochim Acta, 72, 3503–3517, https://doi.org/10.1016/j.gca.2008.04.030, 2008.

Hu, H. and Dominguez, F.: Evaluation of Oceanic and Terrestrial Sources of Moisture for the North American Monsoon Using Numerical Models and Precipitation Stable Isotopes, J Hydrometeorol, 16, 19–35, https://doi.org/10.1175/JHM-D-14-0073.1, 2015.

Jaramillo, C., Ochoa, D., Contreras, L., Pagani, M., Carvajal-Ortiz, H., Pratt, L. M., Krishnan, S., Cardona, A., Romero, M., Quiroz, L., Rodriguez, G., Rueda, M. J., De La Parra, F., Morón, S., Green, W., Bayona, G., Montes, C., Quintero, O., Ramirez, R., Mora, G., Schouten, S., Bermudez, H., Navarrete, R., Parra, F., Alvarán, M., Osorno, J., Crowley, J. L., Valencia, V., and Vervoort, J.: Effects of rapid global warming at the paleocene-eocene boundary on neotropical vegetation, Science, 330, 957–961, https://doi.org/10.1126/science.1193833, 2010.

John, C. M., Bohaty, S. M., Zachos, J. C., Sluijs, A., Gibbs, S., Brinkhuis, H., and Bralower, T. J.: North American continental margin records of the Paleocene-Eocene thermal maximum: Implications for global carbon and hydrological cycling, Paleoceanography, 23, https://doi.org/10.1029/2007PA001465, 2008.

Kemp, S. J., Ellis, M. A., Mounteney, I., and Kender, S.: Palaeoclimatic implications of high-resolution clay mineral assemblages preceding and across the onset of the Palaeocene–Eocene Thermal Maximum, North Sea Basin, Clay Miner, 51, 793–813, https://doi.org/10.1180/CLAYMIN.2016.051.5.08, 2016.

Kiehl, J. T. and Shields, C. A.: Sensitivity of the palaeocene-eocene thermal maximum climate to cloud properties, Philosophical Transactions of the Royal Society A: Mathematical, Physical and Engineering Sciences, 371, https://doi.org/10.1098/rsta.2013.0093, 2013.

Kiehl, J. T., Shields, C. A., Snyder, M. A., Zachos, J. C., and Rothstein, M.: Greenhouse- and orbital-forced climate extremes during the early Eocene, Philosophical Transactions of the Royal Society A: Mathematical, Physical and Engineering Sciences, 376, https://doi.org/10.1098/RSTA.2017.0085, 2018.

Kiehl, J. T., Zarzycki, C. M., Shields, C. A., and Rothstein, M. V.: Simulated changes to tropical cyclones across the Paleocene-Eocene Thermal Maximum (PETM) boundary, Palaeogeogr Palaeoclimatol Palaeoecol, 572, 110421, https://doi.org/10.1016/J.PALAEO.2021.110421, 2021.

Korasidis, V. A., Wing, S. L., Shields, C. A., and Kiehl, J. T.: Global Changes in Terrestrial Vegetation and Continental Climate During the Paleocene-Eocene Thermal Maximum, Paleoceanogr Paleoclimatol, 37, https://doi.org/10.1029/2021PA004325, 2022.

Kozdon, R., Penman, D. E., Kelly, D. C., Zachos, J. C., Fournelle, J. H., and Valley, J. W.: Enhanced Poleward Flux of Atmospheric Moisture to the Weddell Sea Region (ODP Site 690) During the Paleocene-Eocene Thermal Maximum, Paleoceanogr Paleoclimatol, 35, 1–14, https://doi.org/10.1029/2019pa003811, 2020.

Kraus, M. J. and Riggins, S.: Transient drying during the Paleocene-Eocene Thermal Maximum (PETM): Analysis of paleosols in the bighorn basin, Wyoming, Palaeogeogr Palaeoclimatol Palaeoecol, 245, 444–461, https://doi.org/10.1016/j.palaeo.2006.09.011, 2007.

Krishnan, S., Pagani, M., Huber, M., and Sluijs, A.: High latitude hydrological changes during the Eocene Thermal Maximum 2, Earth Planet Sci Lett, 404, 167–177, https://doi.org/10.1016/j.epsl.2014.07.029, 2014.

Liu, B., Yan, Y., Zhu, C., Ma, S., and Li, J.: Record-Breaking Meiyu Rainfall Around the Yangtze River in 2020 Regulated by the Subseasonal Phase Transition of the North Atlantic Oscillation, Geophys Res Lett, 47, https://doi.org/10.1029/2020GL090342, 2020.

Lunt, D. J., Huber, M., Anagnostou, E., Baatsen, M. L., Caballero, R., DeConto, R., ... & Zeebe, R. E. The DeepMIP contribution to PMIP4: Experimental design for model simulations of the EECO, PETM, and pre-PETM (version 1.0). *Geoscientific Model Development*, *10*(2), 889-901, 2017.

Lyons, S. L., Baczynski, A. A., Babila, T. L., Bralower, T. J., Hajek, E. A., Kump, L. R., ... & Freeman, K. H. Palaeocene–Eocene Thermal Maximum prolonged by fossil carbon oxidation. *Nature Geoscience*, *12*(1), 54-60, 2019.

Massoud, E. C., Espinoza, V., Guan, B., and Waliser, D. E.: Global Climate Model Ensemble Approaches for Future Projections of Atmospheric Rivers, Earths Future, 7, 1136–1151, https://doi.org/10.1029/2019EF001249, 2019.

McInerney, F. A. and Wing, S. L.: The Paleocene-Eocene Thermal Maximum: A Perturbation of Carbon Cycle, Climate, and Biosphere with Implications for the Future, Annu Rev Earth Planet Sci, 39, 489–516, https://doi.org/10.1146/annurev-earth-040610-133431, 2011.

Nicolo, M. J., Dickens, G. R., and Hollis, C. J.: South Pacific intermediate water oxygen depletion at the onset of the Paleocene-Eocene thermal maximum as depicted in New Zealand margin sections, Paleoceanography, 25, 1–12, https://doi.org/10.1029/2009PA001904, 2010.

Pagani, M., Pedentchouk, N., Huber, M., Sluijs, A., Schouten, S., Brinkhuis, H., Damsté, J. S. S., Dickens, G. R., Backman, J., Clemens, S., Cronin, T., Eynaud, F., Gattacceca, J., Jakobsson, M., Jordan, R., Kaminski, M., King, J., Koc, N., Martinez, N. C., McInroy, D., Moore, T. C., O'Regan, M., Onodera, J., Pälike, H., Rea, B., Rio, D., Sakamoto, T., Smith, D. C., St John, K. E. K., Suto, I., Suzuki, N., Takahashi, K., Watanabe, M., and Yamamoto, M.: Arctic hydrology during global warming at the Palaeocene/Eocene thermal maximum, Nature, 442, 671–675, https://doi.org/10.1038/nature05043, 2006.

Peters, K.E., Walters, C.C., Moldowan, J.M. The Biomarker Guide: II Biomarkers and Isotopes in Petroleum Systems and Earth History, 2nd edition. Cambridge University Press, Cambridge, 2005.

Risser, M. D. and Wehner, M. F.: Attributable Human-Induced Changes in the Likelihood and Magnitude of the Observed Extreme Precipitation during Hurricane Harvey, Geophys Res Lett, 44, 12,457-12,464, https://doi.org/10.1002/2017GL075888, 2017.

Romero, I. C. and Feakins, S. J.: Spatial gradients in plant leaf wax D/H across a coastal salt marsh in southern California, Org Geochem, 42, 618–629, https://doi.org/10.1016/J.ORGGEOCHEM.2011.04.001, 2011.

Rush, W. D., Kiehl, J. T., Shields, C. A., and Zachos, J. C.: Increased frequency of extreme precipitation events in the North Atlantic during the PETM: Observations and theory, Palaeogeogr Palaeoclimatol Palaeoecol, 568, https://doi.org/10.1016/j.palaeo.2021.110289, 2021.

Sachse, D., Billault, I., Bowen, G. J., Chikaraishi, Y., Dawson, T. E., Feakins, S. J., Freeman, K. H., Magill, C. R., McInerney, F. A., van der Meer, M. T. J., Polissar, P., Robins, R. J., Sachs, J. P., Schmidt, H.-L., Sessions, A. L., White, J. W. C., West, J. B., and Kahmen, A.: Molecular Paleohydrology: Interpreting the Hydrogen-Isotopic Composition of Lipid Biomarkers from Photosynthesizing Organisms, Annu Rev Earth Planet Sci, 40, 221–249, https://doi.org/10.1146/annurev-earth-042711-105535, 2012.

Schmitz, B. and Pujalte, V.: Sea-level, humidity, and land-erosion records across the initial Eocene thermal maximum from a continental-marine transect in northern Spain, Geology, 31, 689–692, https://doi.org/10.1130/G19527.1, 2003.

Self-Trail, J. M., Robinson, M. M., Bralower, T. J., Sessa, J. A., Hajek, E. A., Kump, L. R., Trampush, S. M., Willard, D. A., Edwards, L. E., Powars, D. S., and Wandless, G. A.: Shallow marine response to global climate change during the Paleocene-Eocene Thermal Maximum, Salisbury Embayment, USA, Paleoceanography, 32, 710–728, https://doi.org/10.1002/2017PA003096, 2017.

Shields, C. A. and Kiehl, J. T. Atmospheric river landfall-latitude changes in future climate simulations, Geophys Res Lett, 43, 8775–8782, https://doi.org/10.1002/2016GL070470, 2016.

Shields, C. A., Kiehl, J. T., Rush, W., Rothstein, M., and Snyder, M. A.: Atmospheric rivers in high-resolution simulations of the Paleocene Eocene Thermal Maximum (PETM), Palaeogeogr Palaeoclimatol Palaeoecol, 567, https://doi.org/10.1016/j.palaeo.2021.110293, 2021.

Simon Wang, S. Y., Yoon, J. H., Becker, E., and Gillies, R.: California from drought to deluge, Nature Climate Change 2017 7:7, 7, 465–468, https://doi.org/10.1038/nclimate3330, 2017.

Slotnick, B. S., Dickens, G. R., Nicolo, M. J., Hollis, C. J., Crampton, J. S., Zachos, J. C., and Sluijs, A.: Large-amplitude variations in carbon cycling and terrestrial weathering during the latest Paleocene and earliest Eocene: The record at Mead Stream, New Zealand, Journal of Geology, 120, 487–505, https://doi.org/10.1086/666743, 2012.

Sluijs, A. and Brinkhuis, H.: A dynamic climate and ecosystem state during the Paleocene-Eocene Thermal Maximum: Inferences from dinoflagellate cyst assemblages on the New Jersey Shelf, Biogeosciences, 6, 1755–1781, https://doi.org/10.5194/bg-6-1755-2009, 2009.

Sluijs, A. and Dickens, G. R.: Assessing offsets between the δ13C of sedimentary components and the global exogenic carbon pool across early Paleogene carbon cycle perturbations, Global Biogeochem Cycles, 26, https://doi.org/10.1029/2011GB004224, 2012.

Sluijs, A., Brinkhuis, H., Crouch, E. M., John, C. M., Handley, L., Munsterman, D., Bohaty, S. M., Zachos, J. C., Reichart, G. J., Schouten, S., Pancost, R. D., Damsté, J. S. S., Welters, N. L. D., Lotter, A. F., and Dickens, G. R.: Eustatic variations during the Paleocene-Eocene greenhouse world, Paleoceanography, 23, https://doi.org/10.1029/2008PA001615, 2008.

Smith, F. A., Wing, S. L., and Freeman, K. H.: Magnitude of the carbon isotope excursion at the Paleocene-Eocene thermal maximum: The role of plant community change, Earth Planet Sci Lett, 262, 50–65, https://doi.org/10.1016/j.epsl.2007.07.021, 2007.

Stassen, P., Thomas, E., and Speijer, R. P.: The progression of environmental changes during the onset of the Paleocene-Eocene thermal maximum (New Jersey coastal plain), Austrian Journal of Earth Sciences, 105, 169–178, 2012.

Stevenson, S., Coats, S., Touma, D., Cole, J., Lehner, F., Fasullo, J., and Otto-Bliesner, B.: Twenty-first century hydroclimate: A continually changing baseline, with more frequent extremes, PNAS, 119, https://doi.org/10.1073/pnas, 2022.

Swain, D. L., Langenbrunner, B., Neelin, J. D., and Hall, A.: Increasing precipitation volatility in twenty-first-century California, Nat Clim Chang, 8, 427–433, https://doi.org/10.1038/s41558-018-0140-y, 2018.

Tateo, F.: Clay minerals at the paleocene–eocene thermal maximum: Interpretations, limits, and perspectives, Minerals, 10, 1–16, https://doi.org/10.3390/min10121073, 2020.

Tipple, B. J., Pagani, M., Krishnan, S., Dirghangi, S. S., Galeotti, S., Agnini, C., Giusberti, L., and Rio, D.: Coupled high-resolution marine and terrestrial records of carbon and hydrologic cycles variations during the Paleocene – Eocene Thermal Maximum (PETM), Earth Planet Sci Lett, 311, 82–92, https://doi.org/10.1016/j.epsl.2011.08.045, 2011.

Tipple, B. J., Berke, M. A., Doman, C. E., Khachaturyan, S., and Ehleringer, J. R.: Leaf-wax *n*-alkanes record the plant-water environment at leaf flush, Proc Natl Acad Sci U S A, 110, 2659–2664, https://doi.org/10.1073/pnas.1213875110, 2013.

Tipple, B. J., Berke, M. A., Hambach, B., Roden, J. S., and Ehleringer, J. R.: Predicting leaf wax *n*-alkane 2H/1H ratios: controlled water source and humidity experiments with hydroponically grown trees confirm predictions of Craig–Gordon model, Plant Cell Environ, 38, 1035–1047, https://doi.org/10.1111/PCE.12457, 2015.

Vogel, M. M., Hauser, M., and Seneviratne, S. I.: Projected changes in hot, dry and wet extreme events' clusters in CMIP6 multi-model ensemble, Environmental Research Letters, 15, https://doi.org/10.1088/1748-9326/ab90a7, 2020.

Wakeham, S. G. and Pease, T. K.: Lipid Analysis in Marine Particle and Sediment Samples A Laboratory Handbook, 2004.

Williams, A. P., Cook, E. R., Smerdon, J. E., Cook, B. I., Abatzoglou, J. T., Bolles, K., Baek, S. H., Badger, A. M., and Livneh, B.: Large contribution from anthropogenic warming to an emerging North American megadrought, Science (1979), 368, 314–318, 2020.

Willis, K.J, McElwain, J. C.: The Evolution of Plants, OUP Oxford, 392 pp., 2002.

Wing, S. L., Harrington, G. J., Smith, F. a, Bloch, J. I., Boyer, D. M., and Freeman, K. H.: Transient Floral Change and rapid global warming at the P/E boundary, Science (1979), 310, 993–996, https://doi.org/10.1126/science.1116913, 2005.

Zachos, J. C., Dickens, G. R., and Zeebe, R. E.: An early Cenozoic perspective on greenhouse warming and carbon-cycle dynamics, Nature, 451, 279–283, https://doi.org/10.1038/nature06588, 2008.

Zhu, J., Poulsen, C. J., Otto-Bliesner, B. L., Liu, Z., Brady, E. C., and Noone, D. C.: Simulation of early Eocene water isotopes using an Earth system model and its implication for past climate reconstruction, Earth Planet Sci Lett, 537, 116164, https://doi.org/10.1016/j.epsl.2020.116164, 2020.

Zscheischler, J. and Lehner, F.: Attributing Compound Events to Anthropogenic Climate Change, Bull Am Meteorol Soc, 103, E936–E953, https://doi.org/10.1175/BAMS-D-21-0116.1, 2022.